Hydrogenated surface disorder enhances lithium ion battery performance

Ting Xia,[1] Wei Zhang,[2] Wenjing Li,[1] Nathan A. Oyler,[1] Gao Liu,[2,*] Xiaobo Chen[1,*]

1. Department of Chemistry, University of Missouri – Kansas City, Kansas City, MO 64110, U.S.A.
2. Lawrence Berkeley National Laboratory, University of California at Berkeley, Berkeley, California 94720, U.S.A.

*Corresponding author:

Xiaobo Chen, phone: 816-235-6420, email: chenxiaobo@umkc.edu

Gao Liu, phone: 510-486-7202, email: GLiu@lbl.gov

Abstract

TiO_2, well known for photocatalysis, has also been studied as a safer anode material for lithium ion batteries compared to graphite, while with the limited lithium ion diffusion within the host and the structural distortion during lithium insertion/extraction. Here, we demonstrate that a thin layer of hydrogenated surface disorder on the crystalline TiO_2 electrode may induce better electrochemical energy storage performance, better charge/discharge rate performance, larger capacity and longer stability. The reasons for these improvements are explored in terms of the facilitation of easier lithium ion transport within the disordered layer and the less structural distortion during the lithium insertion/extraction process.

Key words

Titanium dioxide, nanocrystals, disorder, lithium ion battery

Introduction

Titanium dioxide (TiO_2) nanomaterials have been widely studied as photocatalysts [1-4]. Many studies have suggested that anatase phase is more active in many photocatalytic reactions [4,5]. Much effort has been devoted in improving the photocatalytic performance of TiO_2, such as by metal or non-metal doping [6-9], and compositing [10]. Our recent discovery of "black" TiO_2 nanoparticles with long-wavelength optical absorption by hydrogenation has opened a new avenue [11] and triggered great interest [12-17]. Distinct from these approaches, we demonstrated turning white anatase nanocrystals into black TiO_2 by hydrogenation at elevated temperature, by changing the arrangement of the atoms on the surface layers surrounding the crystalline TiO_2 core [11]. The overlap of the oxygen *p*- and titanium *d*-orbitals along with a mixing of the hydrogen *s*-orbitals with those of TiO_2 induces mid-gap electronic levels above the valence band of TiO_2 where the H atoms are partially bonded to both oxygen and titanium atoms [11]. The distinctive feature of the hydrogenated black TiO_2 nanoparticles is its highly disordered surface capping its highly crystalline core. This crystalline/disordered core/shell structure has displayed superior performance in the photocatalytic hydrogenation as photocatalyst due to the better charge separation capability after the light absorption.

TiO_2 has on the other hand been studied as a safer anode material for lithium ion batteries compared to graphite, as the lithium insertion/extraction occurs around 1.5 – 1.8 V vs. Li^+/Li redox couple, while graphite has an operating voltage close to Li electroplating potential [18,19]. Li-reaction with TiO_2 is conveniently expressed as:

$$xLi^+ + TiO_2 + xe^- \leftrightarrow Li_xTiO_2$$

where x is the mole fraction of lithium in the titanium dioxide. TiO_2 can offer a capacity up to its theoretical value at 335 $mAhg^{-1}$ or 1.0 Li per TiO_2. Anatase TiO_2 has a tetragonal body-centered space group $I4_1/amd$, and is comprised of TiO_6 octahedral sharing two adjacent edges with two other octahedral so that planar chains are formed [20]. Li ions diffuse along a path connecting the octahedral interstitial sites in an anatase framework [21,22]. With Li ion insertion, the symmetry of the anatase unit cell decreases and, when x=0.5 ($Li_{0.5}TiO_2$), its original $I4_1/amd$ symmetry transforms into the orthorhombic $Pmn2_1$ space group due to the loss of symmetry in the y direction [23]. The change in symmetry is accompanied by a decrease of the unit cell along the c-axis and an increase along the b-axis, resulting in a net increase of ~4% of the unit cell volume and a rapid capacity fade [24]. As thus, for bulk anatase TiO_2, x = 0.5 is most consistently reported as the maximum electrochemical insertion of Li [25,26]. During Li insertion, the anatase undergoes spontaneous phase separation into $Li_{0.01}TiO_2$ and $Li_{0.6}TiO_2$ domains on a scale of several tens of nanometers [27,28]. Bulk anatase demonstrates flat voltage curves, indicating a classical bi-phase electrochemical reaction process of the Li-insertion/extraction. Decreasing the particle size into the nano-regime alternates the electrochemical reactions and reactivity to Li [29-31]. The Li-interaction with the nanostructures behaves more like solid solution [29]. The size reduction, along with unique morphologies, also leads to increased capacity over 0.5Li per unit formula due to the surface-confined charge storage and different Li-reaction mechanisms from that in the bulk materials.

Here we would like to demonstrate that this surface-disordered structure is also beneficial to the charge transfer process and the capacity retention of the electrodes made

of these materials compared the pure crystalline materials. Figure 1 schematically illustrates this concept. As the overlap of the atomic orbital on the disordered surface layer decreased compared to the crystalline phase, the interaction between the transferred charges and the host matrix can be weaker, thus the charge transport within the electrode material become easier. Due to the more flexible structure in the disordered layer, the charge transfer with the coated conductive carbon can become faster and the smaller structural distortion during the charge/discharge process can allow the larger capacity retention and longer lifetime of the electrode. This concept is hereby demonstrated with the hydrogenated surface-disordered TiO_2 nanocrystals as the active electrode material with a comparative study on pure crystalline TiO_2 nanocrystals to illustrate its benefits.

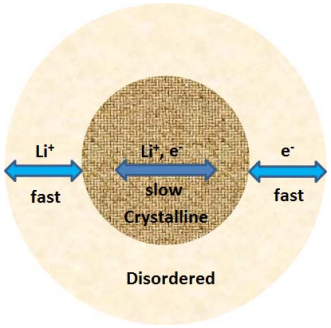

Figure 1. Illustration of surface disordered layer to facilitate the fast charge transfer and the capacity retention.

Material and methods

Materials: titanium tetraisopropoxide, ethanol, hydrochloric acid, deionized water, and Pluronic F127, acetylene black (AB), polyvinylidene fluoride (PVDF), N-methylpyrrolidone (NMP) and 1M lithium hexafluorophosphate ($LiPF_6$) in ethylene carbonate (EC): diethyl carbonate (DEC) (1:2 weight ratio).

Nanocrystal synthesis: Crystalline and surface-disordered TiO_2 nanoparticles were prepared as follows [11]. Briefly, we prepared crystalline TiO_2 nanoparticles with a precursor solution consisting of titanium tetraisopropoxide, ethanol, hydrochloric acid, deionized water, and a polymer template, Pluronic F127. The solution was maintained at 40 °C for 24 hours and then dried at 110 °C. The dried powders were calcinated in air at 500 °C for 6 hours to remove the polymer template and to enhance the crystallization of TiO_2 nanoparticles. The surface-disordered TiO_2 nanoparticles were obtained through the hydrogenation process as follows. The calcinated white-colored powders were placed in a sealed sample chamber under vacuum for 1 hour and then hydrogenated in a 20.0 bar H_2 atmosphere at about 200 ^oC for 5 days.

Nanocrystal characterization: The X-ray diffraction (XRD) patterns were taken on X-ray diffraction patterns were acquired using a Panalytical Xpert Pro diffractometer with monochromatized Cu K_α radiation. The high-resolution transmission electron microscopy (HRTEM) images were taken on a Phillips CM 200 microscope. The electron accelerating voltage was at 200 kV. Small amount of sample was first dispersed in water by sonication. One drop of the aqueous suspension was then dropped onto a thin holey carbon film. The girds were then transferred to an over kept at 60 ºC and dried for overnight before TEM measurement. The FTIR spectra were measured on a Nicolet 6700 FT-IR Spectrometer. All NMR experiments were performed on an 8.45 tesla Oxford magnet with a three channel Tecmag Apollo NMR console, using a home-built, doubly tuned, MAS solid-state NMR probe with a 3.2 mm stator assembly from Revolution NMR. The magic angle spinning (MAS) rate was 12 kHz, the proton excitation pulse during the Bloch decay experiment was ~50 kHz, and the spectra were externally

referenced to adamantane. Each spectrum was acquired with 16 scans and the subtraction was performed after normalizing the peak at ~ 6ppm. Both white and black TiO_2 samples were evacuated at room temperature overnight to remove the surface adsorbed water vapor from the atmosphere.

Electrode preparation: We fabricated half cells in order to test the concept of the stabilization of the lithium insertion and disinsertion with the surface disorder TiO_2 nanocrystals. The fabrication procedure is as follows [33,34]. The materials used in the fabrication of these half cells include acetylene black (AB), polyvinylidene fluoride (PVDF), N-methylpyrrolidone (NMP) and 1M lithium hexafluorophosphate ($LiPF_6$) in ethylene carbonate (EC): diethyl carbonate (DEC) (1:2 weight ratio). The preparation of the TiO_2 electrodes was conducted in an argon-filled glove box. The electrode mixture (82 wt% TiO_2, 8 wt% AB and 10 wt% PVDF) was steadily dispersed in NMP using a Polytron PT10-35 homogenizer at 2700 rpm for 30 minutes. The slurry was cast on a battery-grade copper sheet using a doctor blade. After being dried overnight, the electrodes were punched to 1/2" diam. discs and dried in *vacuo* at 110°C overnight before being assembled into coin cells. The electrode loading was controlled at around 1.4mg TiO_2/cm^2.

Coin cell fabrication and testing: Coin cell assembly was prepared in standard 2325 coin cell hardware under dry argon atmosphere. The separator was from Celgard (product 2400). 1.0 M $LiPF_6$ in 1:2 EC:DEC was used as the electrolyte solution, and lithium as the counter electrode. Cells were discharged to 0.95V and charged to 3.05V after 15min resting for the first cycle at C/25 (calculated from a specific capacity value of 336mAh/g) using a Maccor battery cycler at 30°C. For the 2^{nd} cycle, cells were

discharged to 1.0V and charge to 3.0V at C/5. Then the cells were cycled at 1C from 1.0V to 3.0V. Data were recorded for every 10 mV of voltage change. For rate performance test, for the first 18 cycles, the charge and discharge rates were changed simultaneously; and for the following cycles, only the charging rates changed while the discharge rate was kept at 1C.

Results and Discussions

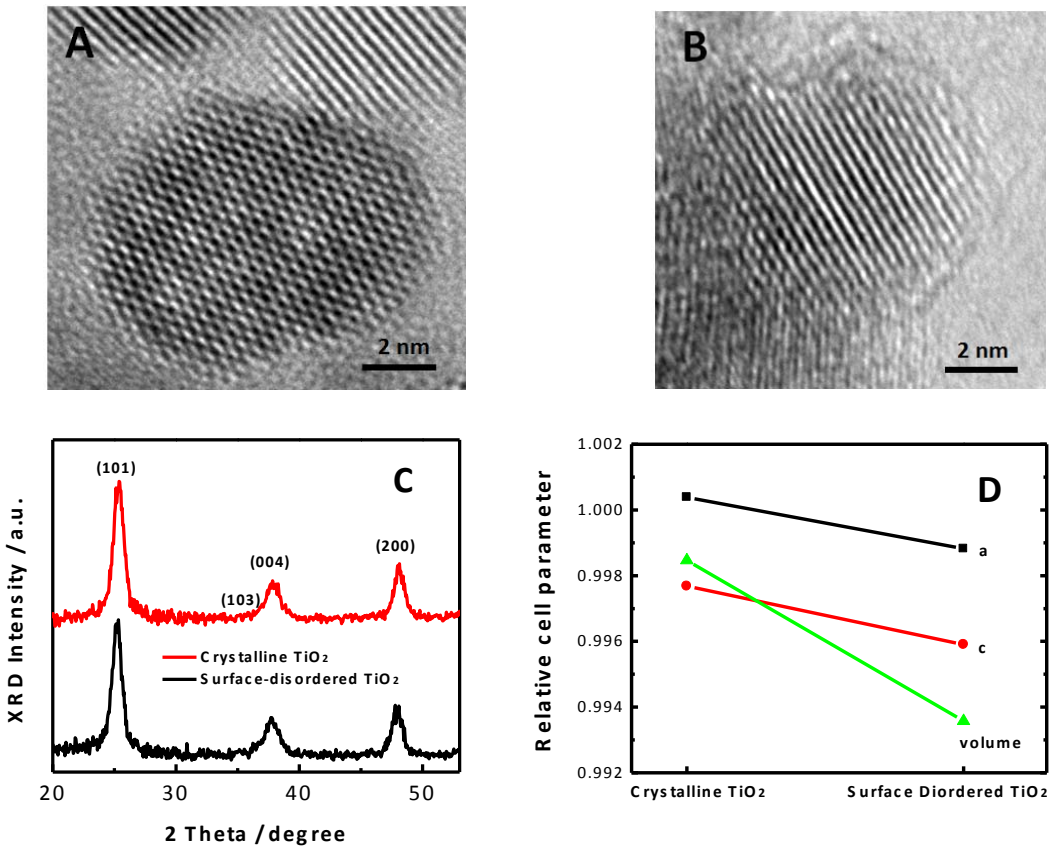

Figure 2. High-resolution transmission electron microscopy images of (A) pristine crystalline and (B) hydrogenated surface-disordered TiO_2 nanocrystals. (C) XRD results of pristine crystalline and hydrogenated surface-disordered TiO_2 nanocrystals. (D) Relative cell parameters a and c, with unite cell volume, of pristine crystalline and

hydrogenated surface-disordered TiO_2 nanocrystals, normalized by the cell parameters of bulk anatase TiO_2.

Figures 2A and 2B show the high-resolution transmission electron microscopy (HRTEM) images of the pure and hydrogenated TiO_2 nanocrystals, respectively. As seen, the sizes of these pure and hydrogenated TiO_2 nanocrystals are around 8 nm in diameter. The pure TiO_2 nanocrystals are highly crystalline throughout the whole particle, while hydrogenated TiO_2 nanocrystal shows crystalline core with a disordered amorphous shell with a few atomic layers' thickness. The thickness of this disordered amorphous shell is around 0.4-1.0 nm, accounting around 14.2%-33.0% of the total volume of the nanoparticle.

The XRD results of pristine white and hydrogenated black TiO_2 nanocrystals are shown in Figure 2C. The strong diffraction peaks suggest that both pure white and hydrogenated black TiO_2 displayed highly crystalline anatase phases. We can deduce the lattice plane spacing and lattice parameters from the Bragg's law $n\lambda = 2dsin\theta$, where n is an integer, λ is the wavelength of incident wave (Cu-Kα, λ = 1.5418 Å), d is the spacing between the planes in the atomic lattice, and θ is the angle between the incident ray and the scattering planes (diffraction angle). The values of plane spacing of planes (101), and (200) of pure white TiO_2 nanocrystals are larger than bulk TiO_2; the values of plane spacing of plane (001) of pure white TiO_2 nanocrystals are smaller than bulk TiO_2. After hydrogenation, all the plane spacing decrease. The values of the plane spacing of all these planes of hydrogenated black TiO_2 nanocrystals are smaller than bulk TiO_2. The lattice plane spacing of {101}, {001}, and {100} of pristine TiO_2 nanocrystal is 3.53 Å, 2.38 Å and 1.90 Å, respectively; lattice plane spacing of {101}, {001}, and {100} of surface

disordered TiO_2 nanocrystal is 3.52 Å, 2.37 Å and 1.89 Å, respectively; apparently, there are 0.42%, 0.17% and 0.16% lattice plane contractions from the disordered TiO_2 nanocrystal. As anatase TiO_2 has tetragonal structure. The lattice plane spacing d between adjacent (hkl) planes has the following relationship with the unit cell parameters: $1/d^2 = (h^2 + k^2)/a^2 + l^2/c^2$, where a and c are the unit cell lengths. With this relationship, we can deduce the unit cell parameters a and c. Furthermore, the change of unit cell parameters a, c and volume of pristine white and hydrogenated black TiO_2 nanocrystals can be obtained by subtracting and normalizing with the bulk values of anatase TiO_2. The results are shown in Figure 2D. Compared to bulk anatase TiO_2 (a: 3.789 Å, c: 9.537 Å, and volume: 136.93 $Å^3$), the unit cell parameter a of pristine white TiO_2 nanocrystals is expanded 0.053% to 3.791 Å, and the unit cell parameter c is contracted 0.23% to 9.515 Å, and the cell volume is contracted 0.15% to 136.72 $Å^3$. For the disordered TiO_2 nanocrystals, the unit cell parameter a, c and cell volume contracted further 0.11% to 3.785 Å, 0.41% to 9.498 Å and 0.64% to 136.05 $Å^3$, respectively. The unit cell parameter a of surface disordered TiO_2 nanocrystals is contracted 0.16%, and the unit cell parameter c is contracted 0.18%, and the cell volume is contracted 0.49%, after the hydrogenation treatment, compared to the pristine TiO_2 nanocrystals.

The crystalline grain size of the anatase was calculated using the Scherrer equation: $\tau = (K\lambda)/(\beta\cos\theta)$, where τ is the mean size of the ordered (crystalline) domains, which may be smaller or equal to the grain size, K is the shape factor with a typical value of 0.9, λ is the X-ray wavelength, β is the line broadening full width at half maximum (FWHM) peak height in radians, and θ is the Bragg angle [32]. The size of crystalline phase of the pristine TiO_2 nanocrystal is 8.31 nm, 6.42 nm and 7.84 nm along (101), (001) and (100)

direction, respectively; while the size of crystalline phase of the surface disordered TiO_2 nanocrystal is 7.84 nm, 6.32 nm and 7.57 nm along (101), (001) and (100) direction, respectively; apparently, the size of the crystalline phase of the surface disordered TiO_2 contracted 5.75% (0.48 nm), 1.50% (0.10 nm), and 3.44% (0.27 nm) long (101), (001) and (100) direction, respectively, after the hydrogenation treatment. As the X-ray diffraction mainly sees the crystalline phase, we can deduce that the amount of the amorphous layer is around 12.3% of the total volume of the nanoparticle. These results are consistent with the HRTEM results shown in Figure 2A and Figure 2B.

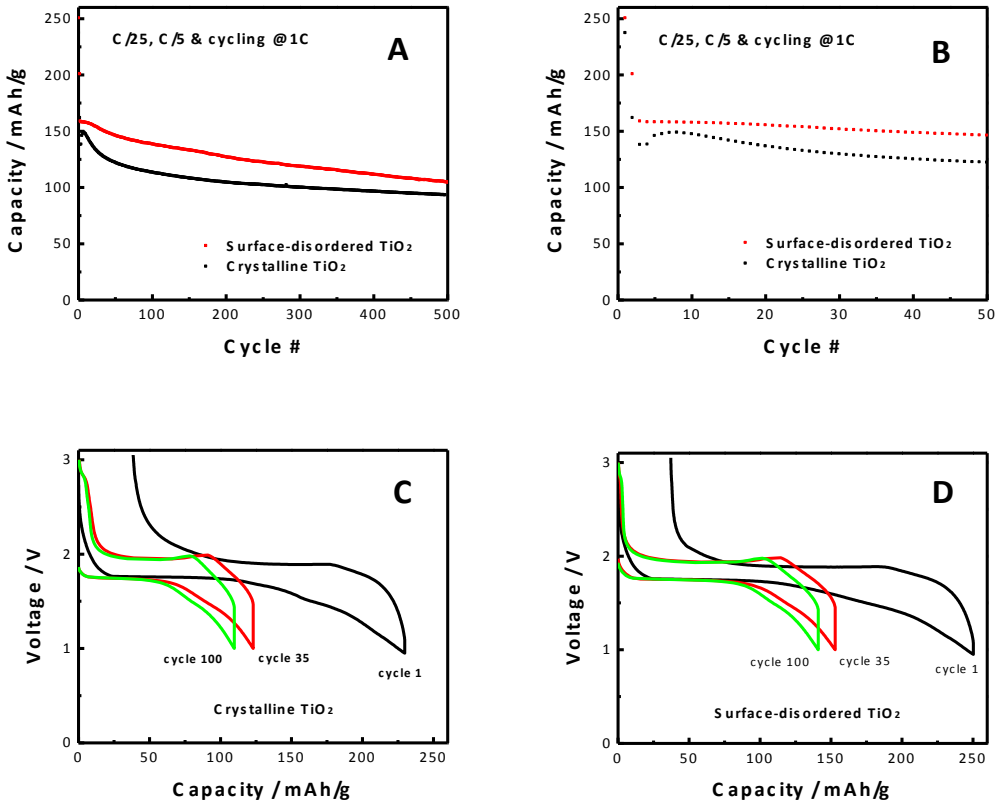

Figure 3. (A) Variation of discharge capacity versus cycle number for the first 500 cycles for pristine crystalline TiO_2 nanocrystals and hydrogenated surface-disordered TiO_2 nanocrystals. The first cycle was conducted at C/25 rate, and the second cycle was

conducted at C/5 rate, and the remaining cycles were conducted at 1C rate. (B) Variation of discharge capacity versus cycle number for the first 50 cycles for electrodes made of pristine crystalline TiO_2 nanocrystals and hydrogenated surface-disordered TiO_2 nanocrystals. (C) Galvanostatic charge/discharge profiles at first cycle at C/25 rate, 35^{th} cycle at 1C rate, and 100^{th} cycle at 1C rate for the electrode made of pristine crystalline TiO_2 nanocrystals. (D) Galvanostatic charge/discharge profiles at first cycle at C/25 rate, 35^{th} cycle at 1C rate, and 100^{th} cycle at 1C rate for the electrode made of the hydrogenated surface-disordered TiO_2 nanocrystals.

The variation of discharge capacity versus cycle number for the first 500 cycles for crystalline TiO_2 nanocrystals and surface-disordered TiO_2 nanocrystals is shown in Figure 3A. The initial discharge capacity of the surface-disordered TiO_2 nanocrystals was 250.20 mAh/g at C/25 rate, 5.5% larger than that of the crystalline TiO_2 nanocrystals (237.17 mAh/g). The second-cycle discharge capacity of the surface-disordered TiO_2 nanocrystals was 200.54 mAh/g at C/5 rate, 24.1% higher than that of the pristine TiO_2 nanocrystals (161.58 mAh/g). The third-cycle discharge capacity of the surface-disordered TiO_2 nanocrystals was 158.68 mAh/g at 1C rate, 15.2% higher than that of the pristine TiO_2 nanocrystals (137.79 mAh/g). After 500 cycles charge/discharges, the discharge capacity of the surface-disordered TiO_2 nanocrystals was 104.71 mAh/g at 1C rate, 12.4% higher than that of the pristine TiO_2 nanocrystals (93.14mAh/g). The discharge capacity of the surface-disordered TiO_2 nanocrystals decreased almost linearly, while the discharge capacity of the crystalline TiO_2 nanocrystals decreased rapidly in the first 150 cycles and then decreased slowly. After the first 150 cycles, the discharge

capacity of the surface-disordered TiO_2 nanocrystals was 132.98 mAh/g at 1C rate, 23.1% higher than that of the crystalline TiO_2 nanocrystals (108.04 mAh/g). Interestingly, for the first 10 charge/discharge cycles, the discharge capacity of the crystalline TiO_2 nanocrystals rapidly decreased and then increased quickly and then decreased slowly in the following cycles as shown in Figure 3B. The galvanostatic charge/discharge profiles at first cycle at C/25 rate, 35^{th} cycle at 1C rate, and 100^{th} cycle at 1C rate for the electrode made of the crystalline TiO_2 nanocrystals and the surface-disordered TiO_2 nanocrystals are shown in Figure 3C and Figure 3D. Besides the larger charge/discharge capacity at various cycles, the surface-disordered TiO_2 nanocrystals show larger charge/discharge plateaus and smaller potential difference between the charge and discharge cycle. For example, the potential difference between the first charge and discharge cycle of the surface-disordered TiO_2 nanocrystals is about 0.11 V, 42.1% smaller than that of the crystalline TiO_2 nanocrystals of about 0.19 V. This smaller potential difference indicates that the decreased transport resistance and weaker chemical bondings between the host matrix and the transferred charges very likely in the disordered layer, which can induce faster ion transport in the disorder layer. The larger charge/discharge plateaus and smaller potential difference of the surface-disordered TiO_2 nanocrystals suggest that the charge transfer is smoother than the crystalline TiO_2 nanocrystals.

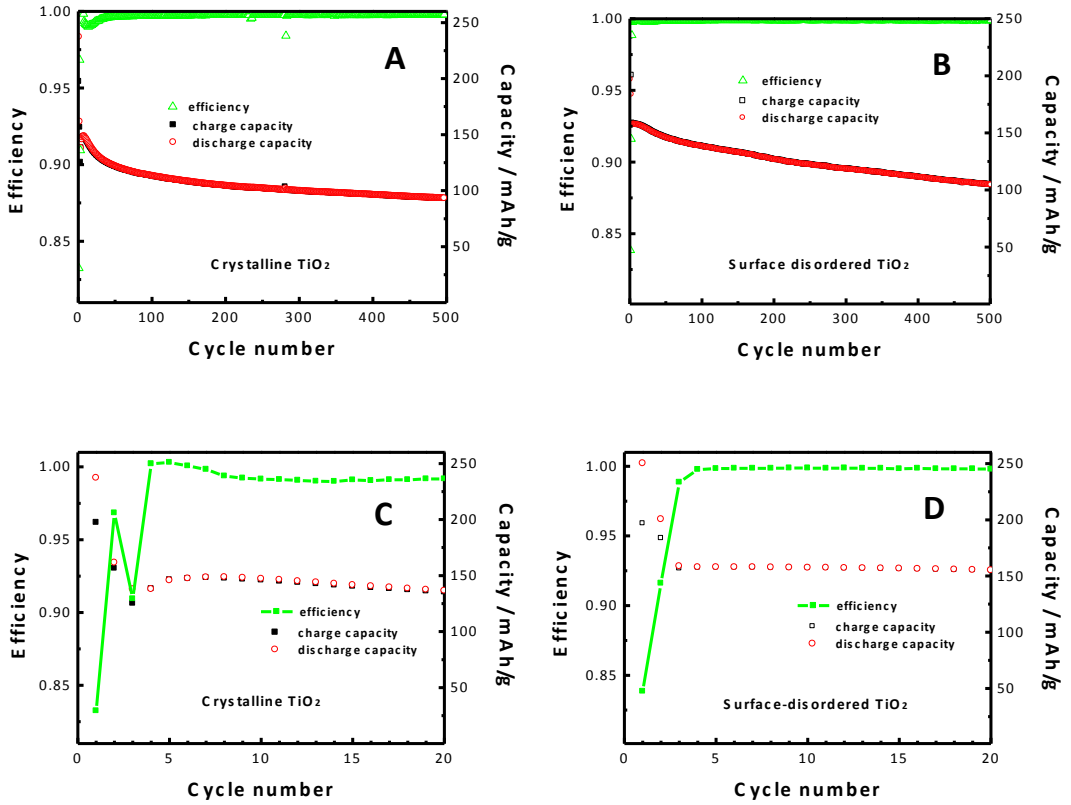

Figure 4. (A) Variation of discharge efficiency along with the charge/discharge versus cycle number for the first 500 cycles for the pristine crystalline TiO_2 nanocrystals. (B) Variation of discharge efficiency along with the charge/discharge versus cycle number for the first 500 cycles for the hydrogenated surface-disordered TiO_2 nanocrystals. (C) Variation of discharge efficiency along with the charge/discharge versus cycle number for the first 20 cycles for the pristine crystalline TiO_2 nanocrystals. (D) Variation of discharge efficiency along with the charge/discharge versus cycle number for the first 20 cycles for the hydrogenated surface-disordered TiO_2 nanocrystals. The first cycle was conducted at C/25 rate, and the second cycle was conducted at C/5 rate, and the remaining cycles were conducted at 1C rate.

The variations of discharge efficiency along with the charge/discharge versus cycle number for the first 500 cycles for the pristine crystalline TiO_2 nanocrystals and the hydrogenated surface-disordered TiO_2 nanocrystals are shown in Figure 4A and Figure 4B. The pristine crystalline TiO_2 nanocrystals show a quick drop of the discharge efficiency in the initial stage followed by a climb-up to the efficiency of around 99.6% after the first 50 cycles which is steady afterward for the remaining 450 cycles (Figure 4A). The hydrogenated surface-disordered TiO_2 nanocrystals show a rapid climb in the initial few cycles to the efficiency of around 99.9% which is steady afterward for the remaining 500 cycles (Figure 4B). A closer look at the first 20 cycles revealed that the discharge efficiency increased with large fluctuation for the pristine crystalline TiO_2 nanocrystals in the first four cycles followed by slight decrease in the next 16 cycles (Figure 4C), while the discharge efficiency of and the hydrogenated surface-disordered TiO_2 nanocrystals increased steadily to the maximum within the first 4 cycles and followed with steady maximum efficiency in the next 16 cycles (Figure 4D). Apparently, the hydrogenated surface-disordered TiO_2 nanocrystals outperformed the pristine crystalline TiO_2 nanocrystals in terms of the coulombic efficiency in the initial cycles.

As seen from the HRTEM image, the disordered surface of the hydrogenated TiO_2 nanoparticles has a large surface roughness. The rougher surface may have edges and corners on the atomic level, which are more favorable for ion adsorption due to the possible surface dangling bonds available. As the surface is disordered, the lattice is poorly defined with thermodynamically metastable energetic state, as compared to the crystalline surface. This will allow better penetration of the lithium ion into the lattice of the host, resulting lower lithium transportation resistance. On the other hand, the solid-

electrolyte surface normally needs to change when lithiation and delithiation happens. The ordered rigid structure of a well-defined surface may not be a good interface in that extensive reorganization may happen which cause the efficiency varies accordingly. Due to large structural distortion tolerance, the disordered surface, on the other hand, may better accommodate the lithium ion insertion/disinsertion (lower voltage difference due to easy lithiation, too) during the lithiation and delithiation processes, so the efficiency is more stable.

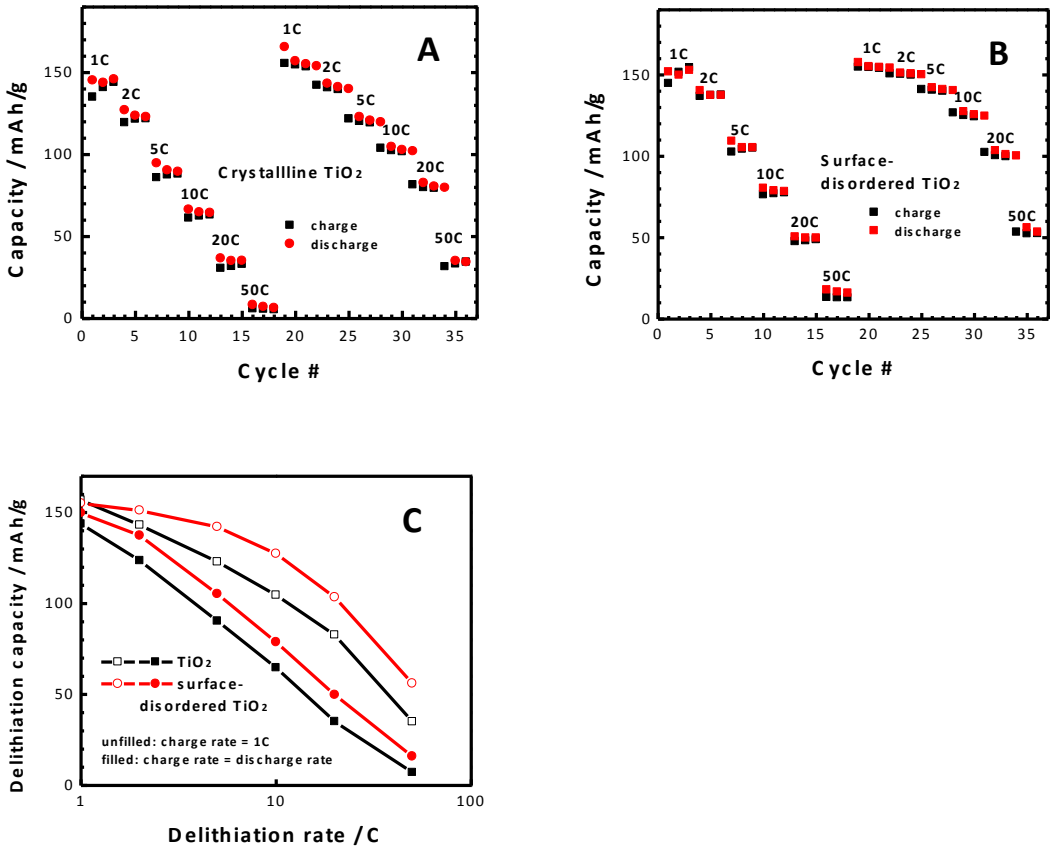

Figure 5. (A) The rate performance of the pristine crystalline TiO_2 nanocrystals. (B) The rate performance of the hydrogenated surface-disordered TiO_2 nanocrystals. In the first 18 cycles, the charge and discharge rates were using the same for each cycle; for the following cycles, the discharge rate was kept at 1C and only the charging rates changed.

(C) Comparison of the discharge capacity of the pristine crystalline TiO_2 nanocrystals and the hydrogenated surface-disordered TiO_2 nanocrystals at various discharge rates.

The rate performance data of the pristine crystalline TiO_2 nanocrystals and the hydrogenated surface-disordered TiO_2 nanocrystals are shown in Figure 5 and Table 1. In the first 18 cycles of the testing, the charge and discharge were using the same rate for each cycle; in the following cycles, the discharge rate was kept at 1C and only the charging rates changed. The mass specific capacity decreases for both samples as the charging/discharging rate increases. For example, the capacity of crystalline TiO_2 decreased from 143.7 mAh/g at 1C to 64.7 at 10C, and 7.05 mAh/g at 50C; the capacity of surface-disordered TiO_2 decreased from 149.8 mAh/g at 1C to 78.7 mAh/g at 10C and 15.9 mAh/g at 50C. Apparently, the surface-disordered TiO_2 nanocrystals show better performance over the crystalline TiO_2 under the same testing condition, i.e. at higher charging/discharging rates. For example, at 50C charge/discharge rate, the surface-disordered TiO_2 displayed 125.5% capacity increase over crystalline TiO_2, when the charge/discharge rate is the same. When the charge/discharge rate is the same, the capacity versus the discharge rate shows an exponential decrease as shown in Figure 5C. When the discharge rate was kept at 1C and only the charging rate was changed, the discharge capacity of both samples increased, compared to when the charging/discharging rates are the same as seen in the cycles 21-39. Again the discharge capacity of the surface-disordered TiO_2 is much higher than that of the crystalline TiO_2. For example, at 50C charging rate, the discharge capacity of the surface-disordered TiO_2 nanocrystal is 56.0 mAh/g, 60% higher than that of the crystalline TiO_2. The higher rate performance of the surface-disordered TiO_2 nanocrystals is possibly due to the lower

energy barrier of the lithium ion transport in the charging and discharging processes in the disordered surface layer [35]. This is in agreement with previous findings on the higher lithium ion higher capacities and capacity retention of amorphous over crystalline TiO_2 nanotubes [36].

Table 1. Rate performance of crystalline and surface-disordered TiO_2 nanocrystals

			C rate					
			1C	2C	5C	10C	20C	50C
Capacity/ mAh/g	1-20 cycles	crystalline	143.7	123.6	90.3	64.7	35.1	7.05
		disordered	149.8	137.4	105.2	78.7	49.8	15.9
	21-30 cycles	crystalline	156.8	143.2	122.9	104.7	82.7	35.0
		disordered	155.0	151.1	142.1	127.4	103.4	56.0

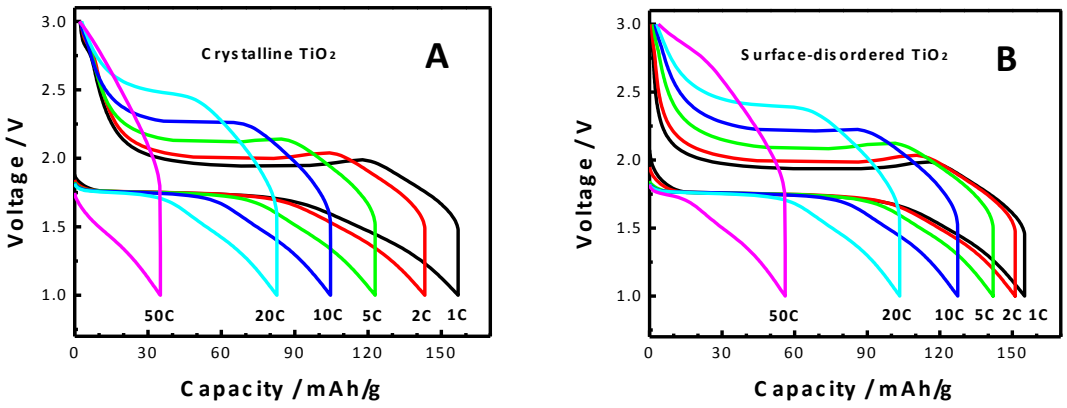

Figure 6. (A) Galvanostatic charge/discharge profiles at various charging rates for the electrode made of pristine crystalline TiO_2 nanocrystals. (B) Galvanostatic charge/discharge profiles at various charging rates for the electrode made of the hydrogenated surface-disordered TiO_2 nanocrystals. The discharge rate was kept at 1C and only the charging rates changed.

Figure 6 shows the galvanostatic charge/discharge profiles at various charging rates for the electrode made of pristine crystalline TiO_2 nanocrystals and hydrogenated

surface-disordered TiO_2 nanocrystals. In general, the surface-disordered TiO_2 nanocrystals show larger capacity at each charging rate over the crystalline TiO_2. Besides, the surface-disordered TiO_2 nanocrystals show larger charge/discharge plateaus between the charge and discharge cycle at each charging rate. The larger charge/discharge plateaus indicates that the smoother charge transport in the disordered layer due to the weaker chemical bondings between the host matrix and the transferred charges.

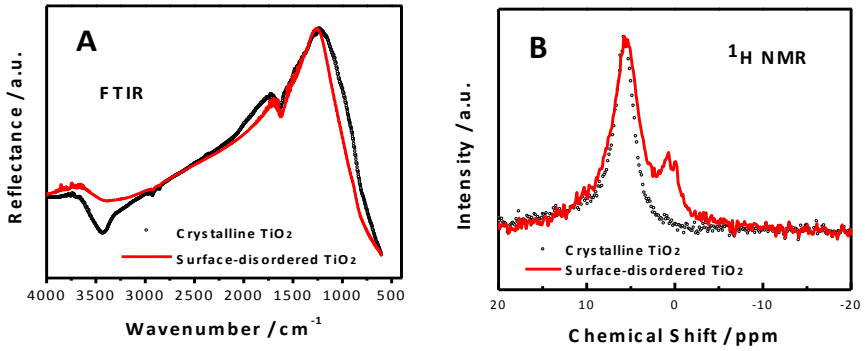

Figure 7. (A) FTIR reflectance spectra of hydrogenated surface-disordered TiO_2 (red line) compared with crystalline TiO_2 (black line) nanocrystals. (B), ^1H magic angle NMR spectra of hydrogenated surface-disordered TiO_2 (red line) compared with crystalline TiO_2 (black line) nanocrystals.

In order to understand why hydrogenated surface disorder can help the lithium ion diffusion across the interface, we have performed an FTIR study of both hydrogenated surface-disordered and crystalline TiO_2 nanocrystals to reveal their surface properties. The results are shown in Figure 7A. Both exhibit OH absorption bands near the 3400 cm^{-1} region, due to a bridging OH group possessing acidic properties [37]. The peaks at around 3730 cm^{-1} and the 3640 cm^{-1} are due to the O-H stretching and wagging modes [37]. The strength of the terminal O-H mode is reduced after crystalline TiO_2 is converted

to hydrogenated surface-disordered TiO_2. This reduction suggests that the hydrogen incorporated into the TiO_2 does not passivate a significant number of O dangling bonds. The wider OH absorption band of the black TiO_2 suggests that the OH groups experience a more varied environment on the surface-disordered TiO_2 surface than on the crystalline surface of the white TiO_2. The linewidth difference may, in addition to the inhomogeneous effect referred to above, come in part from homogeneous (lifetime) broadening due to rapid exchange among sites. Such exchange could provide much faster hydrogen diffusion rate from the surface to the bulk. Since proton and lithium ion exchange were observed in the lithium intercalation materials, this faster hydrogen diffusion rate suggests that the lithium ion diffusion rate is faster in the hydrogenated TiO_2 compared to the crystalline TiO_2 during the lithiation/delithiation processes, as the hydrogen can be easily replaced with the lithium ion. It is thus not strange to see the better charge/discharge rate performance of the hydrogenated surface-disorder TiO_2 nanocrystals.

The high mobility of the hydrogen in the hydrogenated surface-disordered TiO_2 nanocrystals is verified in our nuclear magnetic resonance (NMR) study. The results are shown in Figure 7B. Both hydrogenated surface-disordered and crystalline TiO_2 show a large peak at a chemical shift of +5.7 ppm. The slightly larger linewidth in black TiO_2 may be caused by the incorporation of H at bridging sites at the rutile-like phase produced during the hydrogenation process or may be due to the bridging sites located on different crystallographic planes on the surface [37]. Compared to white TiO_2, black TiO_2 shows two additional narrow peaks at chemical shifts of 0.73 ppm and -0.03 ppm. The sharpness of these additional ^1H NMR resonances suggests that the hydrogen

concentration is low and, in addition, there are dynamical exchanges between ^{1}H in the different environments. Some examples of such dynamical exchange mechanisms are rapid isotropic diffusion and rapid exchange between different proton environments [38,39]. These two peaks are associated with H located in the disordered surface layer of the black TiO_2 as a result of hydrogenation. Thus the presence of disordered surface layer of black TiO_2 may provide an explanation for the enhanced hydrogen mobility in black TiO_2. The higher hydrogen mobility in the hydrogenated TiO_2 suggest that the lithium ion mobility is higher compared to the crystalline TiO_2 during the lithiation/delithiation processes, as the hydrogen can be easily replaced with the lithium ion. This is consistent with the higher lithium ion battery performance with the hydrogenated TiO_2 nanocrystals.

As Lu et al. recently demonstrated that that hydrogenation of TiO_2 nanotubes improves significantly their electrochemical performance as electrode materials for supercapacitors [40]. The enhancement in capacitance was proposed due to the combined contribution from the improved donor density and the increased density of surface hydroxyl groups [40]. Shin et al. reported oxygen-deficient $TiO_{2-\delta}$ nanoparticles prepared by hydrogen reduction displayed the high rate capability of lithium storage and found that well-balanced Li^{+}/e^{-} transport is the key factor for high-performance TiO_2 anodes [41]. Sun et al. found that anatase TiO_2 having different percentages of (001)/(101) surface demonstrated different behaviors for Li^{+} ions insertion and much enhanced rate performance of Li-ion batteries [42]. Aschauer and Selloni recently suggested from density functional theory calculations subsurface oxygen vacancies on reduced anatase are favorable adsorption sites for hydrogen atoms [43]. These oxygen vacancies could also be the reason for the improved lithium ion battery performance of the surface-

disordered TiO_2 electrode in this study. Here we would like to provide one more alternative explanation on the improvement of the electrical energy storage with the surface-disordered TiO_2 nanocrystalline electrode. Previous study showed that, the symmetry of the anatase unit cell decreases with Li ion insertion [23] and the change in symmetry is accompanied by a decrease of the unit cell along the c-axis and an increase along the b-axis, resulting in a net increase of ~ 4% of the unit cell volume and a rapid capacity fade [24]. Based on the previous XRD analysis, the unit cell parameter a, c and cell volume contracted 0.11% to 3.785 Å, 0.41% to 9.498 Å and 0.64% to 136.05 $Å^3$, respectively, for the disordered TiO_2 nanocrystals, when compared with bulk TiO_2. The large structural distortion due to the increase of the unit cell volume and the unit cell length upon the insertion of lithium ion into the unit cell is thus relieved to some extent due to the structural alteration in the surface-disordered TiO_2 nanocrystals from the hydrogenation process. This stress release may cause better structural stability of the TiO_2 host for the lithium ion insertion/extraction process.

Conclusions

In a summary, we have demonstrated here that the surface-disordered structure induced by the hydrogenation process on crystalline TiO_2 nanocrystals can facilitate the charge transfer efficiency and capacity retention efficiency of the pure crystalline electrode. Discharge efficiency near 100% can be obtained for 500 cycles without any degradation. Improvement of the discharge capacity and high-rate charge/discharge is obviously achieved in the 500 cycle test. The faster ion exchange and mobility in the hydrogenated disordered surface may provide the explanation of the better facilitate the

charge transfer efficiency and capacity retention efficiency, besides the large structural tolerance in the disordered surface. This concept of the surface-disordered structure on the outer layer of crystalline electrode materials provides an alternative solution in our searching for high performance electrode materials.

Acknowledgements

X.C. thanks Samuel S. Mao at Lawrence Berkeley National Laboratory for helping on the hydrogenation of the TiO_2 nanocrystals. X.C. thanks the support from College of Arts and Sciences, University of Missouri - Kansas City, the University of Missouri Research Board, and the generous gift from Dow Kokam. TEM work was performed at the National Center for Electron Microscopy, which is supported by the Office of Science, Office of Basic Energy Sciences of the U.S. Department of Energy. G. L. thanks the fund by the Assistant Secretary for Energy Efficiency, Office of Vehicle Technologies of the U.S. DOE under Contract No. DE-AC03-76SF00098.

References

1. A. Fujishima, K. Honda, Electrochemical photolysis of water at a semiconductor electrode, Nature 238 (1972) 37-38.
2. A. Fujishima, T. N. Rao, D. A. Tryk, Titanium dioxide photocatalysis, Journal of Photochemistry and Photobiology C: Photochemistry 1 (2000), 1-21.
3. A. Hagfeldtt, M. Gratzel, Light-induced redox reactions in nanocrystalline systems, Chemical Reviews 95 (1995) 49-68.

4. X. Chen, S. S. Mao, Titanium dioxide nanomaterials: synthesis, properties, modifications, and applications, Chemical Reviews 107 (2007) 2891-2959.
5. U. Diebold, The surface science of titanium dioxide, Surface Science Reports. 48 (2003) 53-229.
6. W. Choi, A. Termin, M. R. Hoffmann, The role of metal ion dopants in quantum-sized TiO_2: correlation between photoreactivity and charge carrier recombination dynamics, The Journal of Physical Chemistry 98 (1994) 13669-13679.
7. M. Anpo, M. Takeuchi, The design and development of highly reactive titanium oxide photocatalysts operating under visible light irradiation, Journal of Catalysis 216 (2003) 505-516.
8. R. Asahi, T. Morikawa, T. Ohwaki, K. Aoki, Y. Taga, Visible-light photocatalysis in nitrogen-doped titanium oxides, Science 293 (2001) 269-271.
9. X. Chen, C. Burda, The electronic origin of the visible-light absorption properties of C-, N- and S-doped TiO_2 nanomaterials, Journal of the American Chemical Society 130 (2008) 5018-5019.
10. J. Zhang, Q. Xu, Z. Feng, M. Li, C. Li, Importance of the relationship between surface phases and photocatalytic activity of TiO2, Angewandte Chemie International Edition 47 (2008) 1766-1769.
11. X. Chen, L. Liu, P. Y. Yu, S. S. Mao, Increasing solar absorption for photocatalysis with black hydrogenated titanium dioxide nanocrystals, Science 331 (2011) 746-750.
12. U. Diebold, Photocatalysts: Closing the gap, Nature Chemistry 3 (2011) 271-272.
13. X. Chen, C. Li, M. Grätzel, R. Kostecki, S. S. Mao, Nanomaterials for renewable energy production and storage, Chemical Society Reviews 41 (2012) 7909.

14. J. Lu, Y. Dai, H. Jin, B. Huang, Effective increasing of optical absorption and energy conversion efficiency of anatase TiO_2 nanocrystals by hydrogenation, Physical Chemistry Chemical Physics 13 (2011) 18063-18068.
15. H. Pan, Y.-W. Zhang, V. B. Shenoy, H. Gao, Effects of H-, N-, and (H, N)-doping on the photocatalytic activity of TiO_2, The Journal of Physical Chemistry C 115 (2011) 12224-12231.
16. O. A. Syzgantseva, P. Gonzalez-Navarrete, M. Calatayud, S. Bromley, C. Minot, Theoretical investigation of the hydrogenation of $(TiO_2)_N$ clusters (N = 1-10), The Journal of Physical Chemistry C 115 (2011) 15890-15899.
17. G. Wang, H. Wang, Y. Ling, Y. Tang, X. Yang, R. C. Fitzmorris, C. Wang, J. Z. Zhang, Y. Li, Hydrogen-treated TiO_2 nanowire arrays for photoelectrochemical water splitting, Nano Lett. 11 (2011) 3026-3033.
18. S. Sodergren, H. Siegbahn, H. Rensmo, H. Lindstom, A. Hagfeldt, S.E. Lindquist, Lithium intercalation in nanoporous anatase TiO_2 studied with XPS, The Journal of Physical Chemistry B 101 (1997) 3087 - 3090.
19. A. Henningsson, H. Rensmo, A. Sandell, H. Siegbahn, S. Sodergren, H. Lindstrom, A. Hagfeldt, Electronic structure of electrochemically Li-inserted TiO_2 studied with synchrotron radiation electron spectroscopies. The Journal of Chemical Physics 118 (2003) 5607 - 5612.
20. C. J. Howard, T. M. Sabine, F. Dickson, Structural and thermal parameters for rutile and anatase, *Acta Crystallographica Section B*: Structural *Science* 47 (1991) 462-468.

21. F. Tielens, M. Calatayud, A. Beltran, C. Minot, J. Andres, Lithium insertion and mobility in the TiO_2-anatase/titanate structure: A periodic DFT study, Journal of Electroanalytical Chemistry 581 (2005) 216–223.
22. S. Lunell, A. Stashans, L. Ojamae, H. Lindstrom, A. Hagfeldt, Li and Na diffusion in TiO_2 from quantum chemical theory versus electrochemical experiment, Journal of the American Chemical Society 119 (1997) 7374–7380.
23. R. J. Cava, D. W. Murphy, S. Zahurak, A. Santoro, R. S. Roth, The crystal structures of the lithium-inserted metal oxides $Li_{0.5}TiO_2$ anatase, $LiTi_2O_4$ spinel, and $Li_2Ti_2O_4$. Journal of Solid State Chemistry 53 (1984) 64-75.
24. G. Sudant, E. Baudrin, D. Larcher, J.-M. Tarascon, Electrochemical lithium reactivity with nanotextured anatase-type TiO_2, Journal of Materials Chemistry 15 (2005) 1263–1269.
25. H. Lindström, S. Södergren, A. Solbrand, H. Rensmo, J. Hjelm, A. Hagfeldt, S.-E. Lindquist, Li^+ ion insertion in TiO_2 (Anatase). 2. Voltammetry on nanoporous films, The Journal of Physical Chemistry B 101 (1997) 7717–7722.
26. R. van de Krol, A. Goossens, E.A. Meulenkamp, In Situ X-Ray Diffraction of lithium intercalation in nanostructured and thin film anatase TiO_2, Journal of the Electrochemical Society 146 (1999) 3150–3154.
27. M. Wagemaker, A. P. M. Kentgens, F. M. Mulder, Equilibrium lithium transport between nanocrystalline phases in intercalated TiO_2 anatase, Nature 418 (2002) 397–399.

28. M. Wagemaker, R. van de Krol, A.P.M. Kentgens, A.A. van Well, F.M. Mulder, Two phase morphology limits lithium diffusion in TiO_2 (anatase): a ^7Li MAS NMR study, Journal of the American Chemical Society 123 (2001) 11454–11461.
29. M. Wagemaker, W.J.H. Borghols, F.M. Mulder, Large impact of particle size on insertion reactions. A case for anatase Li_xTiO_2, Journal of the American Chemical Society 129 (2007) 4323–4327.
30. L. Kavan, M. Kalbac, M. Zukalova, I. Exnar, V. Lorenzen, R. Nesper, M. Graetzel, Lithium storage in nanostructured TiO_2 made by hydrothermal growth, Chemistry of Materials 16 (2004) 477–485.
31. J. Kim, J. Cho, Rate characteristics of anatase TiO_2 nanotubes and nanorods for lithium battery anode materials at room temperature. Journal of the Electrochemical Society 154 (2007) A542–A546.
32. Jenkins, R.; Snyder, R. L.: Introduction to X-ray Powder Diffractometry, John Wiley & Sons Inc., New York, 1996.
33. S. Xun, X. Song, M. E. Grass, D. K. Roseguo, Z. Liu, V. S. Battaglia, G. Liu, Improved initial performance of Si nanoparticles by surface oxide reduction for lithium-ion battery application, Electrochemical and Solid-State Letters 14 (2011) A61-A63.
34. G. Liu, S. Xun, N. Vukmirovic, X. Song, P. Olalde-Velasco, H. Zheng, V. S. Battaglia, L. Wang, W. Yang, Polymers with tailored electronic structure for high capacity lithium battery electrodes, Advanced Materials 23, (2011) 4679-4683.

35. H. Morimoto, H. Yamashita, M. Tatsumisago, T. Minami, Mechanochemical synthesis of new amorphous materials of $60Li_2S{\cdot}40SiS_2$ with high lithium ion conductivity, Journal of the American Ceramic Society 82 (1999) 1352-1354.
36. D. Guan, C. Cai, Y. Wang, Amorphous and crystalline TiO_2 nanotube arrays for enhanced Li-ion intercalation properties, Journal Nanoscience and Nanotechnology 11 (2011), 3641-3650.
37. M. Cracker, R. H. M. Herold, A. E. Wilson, M. Mackay, C. A. Emeis, A. M. Hoogendoorn. ^1H NMR spectroscopy of titania - chemical shift assignments for hydroxy groups in crystalline and amorphous forms of TiO_2. Journal of the Chemical Society, Faraday Transactions 92 (1996) 2791-2798.
38. P. Jonsen, Identification of different hydrogen-reduced titania crystallographis forms by ^1H NMR spectroscopy. Catalysis Letters 2 (1989) 345-350.
39. P. Jonsen, A ^1H NMR study of reduced Ru/TiO_2 and TiO_2. Colloids and Surfaces 36 (1989) 127-132.
40. X. Lu, G. Wang, T. Zhai, M. Yu, J. Gan, Y. Tong, Y. Li, Hydrogenated TiO_2 nanotube arrays for supercapacitors, Nano Letters 12 (2012) 1690-1696.
41. J. -Y. Shin, J. H. Joo, D. Samuelis, J. Maier, Oxygen-deficient $TiO_{2-\delta}$ nanoparticles via hydrogen reduction for high rate capability lithium batteries, Chemistry of Materials 24 (2012) 543-551.
42. C. H. Sun, X. H. Yang, J. S. Chen, Z. Li, X. W. Lou, C. Li, S. C. Smith, G. Q. (Max) Lu, H. G. Yang, Higher charge/discharge rates of lithium-ions across engineered TiO_2 surfaces leads to enhanced battery performance, Chemical Communications 46 (2010) 6129-6131.

43. U. Aschauer, A. Selloni, Hydrogen interaction with the anatase TiO_2 (101) surface, Physical Chemistry Chemical Physics 14 (2012) 16595-16602.

Ting Xia is currently a PhD student working with Professor Xiaobo Chen at the Department of Chemistry, University of Missouri – Kansas City. She obtained her Master degree from Zhejiang University in 2008 and BS degree from Nanjing University of Technology in 2006. She has been working on nanomaterial-based photocatalysis, electrodes and diagnosis of lithium ion batteries with electrochemical impedance spectroscopy.

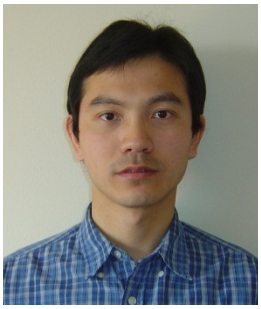

Wei Zhang is a postdoctoral research fellow in the Environmental Energy Technologies Division (EETD) at Lawrence Berkeley National Laboratory (LBNL). He received his PhD degree in the area of organometallic synthesis and coordination polymerization from the department of Chemistry at the University of Maryland - College Park in 2008. He continued his efforts on organometallic catalysis for his first postdoc work in the department of chemistry at the University of California – Berkeley before his joined EETD. His current interests expand to electrochemistry and battery engineering.

Gao Liu is a Staff Scientist and Principal Investigator in the Environmental Energy Technologies Division of Lawrence Berkeley National Laboratory (LBNL). He received a Ph.D. in Chemistry from Michigan State University in 2001. Dr. Liu joined the Batteries for Advanced Transportation Technologies

(BATT) program at LBNL as a postdoctoral fellow in 2001, and became a scientist in 2004. His research work focuses on high-energy lithium battery for transportation applications.

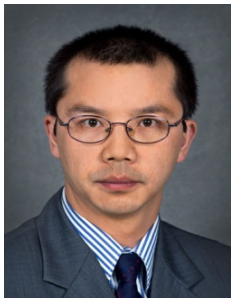

Xiaobo Chen is an Assistant Professor and the Director of Materials Modification and Characterization Laboratory at the Department of Chemistry, University of Missouri – Kansas City (UMKC). He obtained his Ph.D degree from Case Western Reserve University in 2005. His research interests include nanomaterials synthesis, characterization, modifications, and applications in renewable energies, such as photocatalysis, battery and environmental pollution removal. He has published around 40 peer-reviewed articles with over 8000 citations.